Dynamic Behavior of Vertically Aligned Carbon Nanotube Foams With Patterned Microstructure**

By *Ludovica Lattanzi, Ramathasan Thevamaran, Luigi De Nardo* and *Chiara Daraio**

Article first published online: April 22, 2015
Manuscript Received: December 17, 2014
Manuscript Revised: February 24, 2015

1. Introduction

Understanding the structure–property relationship in ordered, multiscale, structured materials is essential to design and create new materials with tunable bulk properties.[1] Nature offers abundant examples in which the choice of specific hierarchical organizations and constituent geometries leads to materials that optimally combine strength, toughness, and stiffness.[2,3] These biological materials have been inspiring the design and fabrication of synthetic micro- and nano-structured materials with novel mechanical behaviors.[4] Synthetic cellular materials, such as honeycombs and open/closed cell foams, are widely used in structural applications due to their lightweights and high strengths.[5] Compared to conventional foams, architected materials (also referred to as "mechanical metamaterials") allow for the reduction of the cell size down to the nanoscale and can be engineered in ordered arrays and geometries.[4] The control of structural architectures at different length scales allows the fabrication of materials with novel properties.[4] For example, introducing order and hierarchy in metallic microlattices improved their mechanical properties significantly, while maintaining very low densities ($\sim 9 \times 10^{-4}\,\mathrm{g\,cm^{-3}}$).[6] This was achieved by designing their microstructure in a periodic array of hollow tubes forming an octahedral unit cell, with feature sizes ranging from nanometer to millimeter.[6] Using hierarchical design principles, similar three-dimensional hollow ceramic nanostructures have been fabricated and shown to combine lightweight with high damage tolerance.[7] The structural design at different length scales also improves the energy absorption capability that is critical for protective materials.[8]

The effect of structural hierarchy on the resultant bulk material properties has also been studied for carbon nanotube structures.[9] CNT foams provide a broad design space to engineer structures at the nano- and micro-scales that can influence the bulk mechanical properties. As such, CNTs can serve as model materials to study fundamental rules for structure–property relations that govern the mechanical responses. The compressive behavior of vertically aligned carbon nanotube (VACNT) forests under quasi-static conditions has been extensively studied, and reported a foam-like response with almost full recovery of large deformations.[9–15] Recently, the effects of bulk density,

[*] *C. Daraio, L. Lattanzi, R. Thevamaran*
Division of Engineering and Applied Sciences, California Institute of Technology, Pasadena, CA 91125, USA
L. Lattanzi, L. De Nardo
Department of Chemistry, Materials, and Chemical Engineering "G. Natta", Politecnico di Milano, Milano 20131, Italy
C. Daraio
Department of Mechanical and Process Engineering, Swiss Federal Institute of Technology, Zurich 8092, Switzerland
E-mail: daraio@ethz.ch

[**] *The authors acknowledge the financial support from the Institute for Collaborative Biotechnologies (ICB) under the contract W911NF-09-D-0001 with the Army Research Office (ARO). L. Lattanzi and L. De Nardo acknowledge INSTM. The authors thank the Kavli Nanoscience Institute at Caltech for the use of nanofabrication facilities. (Supporting Information is available online from Wiley InterScience or from the author).*

microstructure, and the intrinsic density gradient on the bulk dynamic response of the VACNT foams, and their strain rate sensitive fundamental deformation mechanisms have also been investigated in detail.[16] It has been shown that the VACNT foams have the highest modulus for a given density compared to other structures, and their moduli exhibit a power law dependency on density.[16] Their deformation response strongly depends on the impact velocity (and strain rate); they exhibit progressive sequential buckling, governed by their intrinsic density gradient at low velocity of impacts, and they support shock formation beyond a critical velocity of impact, which is a function of the foam's bulk density.[16] Because of their high compressive strength (peak stress), their high energy absorption, and their low densities, vertically aligned CNT forests have been suggested as vibration damping layers[17] or shock and impact absorbers for electronics and space applications.[12]

In an earlier work, we studied the effects of microstructural organization on the quasi-static mechanical response of CNT foams.[9] We designed and fabricated micropatterned CNT foams composed of different 2D lattices: circles, lines, and concentric rings. Quasi-static compression tests of those structures showed that the patterning geometry played a fundamental role in determining the foam's bulk energy absorption, peak stress, and recovery from deformation. Selected micropattern's geometries lead to the fabrication of lighter materials, which preserved the same mechanical response of bulk CNT foams.[9] Lightweight materials having high energy absorption are widely studied for space applications and transport industry, in order to improve safety and fuel economy.[18] Despite extensive studies on the mechanics of CNT foams, the dynamic response of these materials has not been fully characterized.[9–15,19] In particular, understanding their deformation modes and energy dissipation mechanisms during impact is important to build reliable and robust structures usable in applications. In this paper, we describe the impact response of micropatterned CNT foams to characterize their high-rate deformation and their energy absorption capability. We show how the microstructural geometries influence the stress–strain response and the impact performance.

2. Results and Discussion

To study the role of different patterns' geometry on the impact response of CNT structures, we fabricated 7 different micropatterned VACNT foams, classified as: 1D, 2D periodic, and complex structures (Figure 1). For 1D periodic line structures, we varied the gap between the 100 μm thick lines (2 and 50 μm) creating two different micropatterned VACNT foams. For 2D periodic pillar structures, we varied (i) the diameter of the pillars (100 and 200 μm) while keeping the gap constant at 50 μm and (ii) the gap between the pillars (2 and 50 μm) while keeping the diameter of the pillars constant at 100 μm. The orthogonal lines—a 2D periodic array of 100 μm thick lines—have 50 μm gap between the lines. The complex structure—a 2D periodic array of concentric rings made of 20 μm thick rings spaced at a gap of 20 μm has the center-to-center distance of 220 μm.

Loading modulus, peak stress, maximum deformation (strain), and energy dissipation calculated from the dynamic stress–strain curves for all the seven VACNT foams tested are summarized in Table 1. We also used a "control" VACNT foam sample for comparison. All these material parameters correspond to an impact velocity of $0.95\,\mathrm{m\,s^{-1}}$ (impact energy = 2.35 mJ; impact momentum = 4.94 mN s). Table 1 reports the effective density and the theoretical density of the different patterns. The effective density (ρ_{measured}) of the samples is obtained by dividing the measured weight of carbon nanotubes by the measured total volume of the sample. The theoretical effective density ($\rho_{\mathrm{theoretical}}$) of the samples is given by the product between the bulk density of the VACNT forest and the filling fraction of the patterns. The results show discrepancies between the measured effective density and the corresponding theoretical prediction, with $\rho_{\mathrm{theoretical}} > \rho_{\mathrm{measured}}$. Interestingly, the trend changes ($\rho_{\mathrm{theoretical}} < \rho_{\mathrm{measured}}$) when the diameter of the pillars is doubled (from 100 to 200 μm). Even though the pattern made by pillars with 200 μm diameter should have lower density than the pattern made by concentric rings—as also observed in Figure 1—it is not confirmed by the measured effective density. We hypothesize that the pattern's geometry affects the CNT growth process, causing such difference between the effective and the theoretical density. Here, we do not attempt to investigate the morphology of the individual CNTs inside different patterns and leave it for future work.

Figure 2a shows the dynamic mechanical response of both non-patterned (VACNT forest) and patterned (lines, pillars, and concentric ring columns) structures impacted with a striker velocity of $0.95\,\mathrm{m\,s^{-1}}$. The results clearly demonstrate that density plays a marginal role on determining the overall dynamic material's response while the microstructural organization has a fundamental influence on the constitutive behavior. Despite their low effective density ($0.032 \pm 0.02\,\mathrm{g\,cm^{-3}}$), the structures composed of concentric ring columns exhibit the highest stiffness, with a compressive modulus of ~7 MPa. Such modulus is higher than that of non-patterned VACNT structures (~4.4 MPa), which have an order of magnitude higher density ($0.24\,\mathrm{g\,cm^{-3}}$). As previously reported, the wide range of effective density measured for both non-patterned and patterned structures depends on the position of the silicon wafer inside the furnace during the synthesis process.[9,20] Samples closer to the entrance of the feed solution exhibited higher density.[20] VACNT samples patterned with structures having density values ranging from 0.08 to $0.19\,\mathrm{g\,cm^{-3}}$—e.g., pillars with 100 μm diameters and 2 μm gaps, 100 μm thick lines separated by 2 μm gaps, and pillars with 200 μm diameters and 50 μm gaps, and orthogonal lines—undergo larger deformation than the samples patterned with concentric rings.

Results show that by changing the microstructural organization of CNTs, it is possible to tune the stress–strain

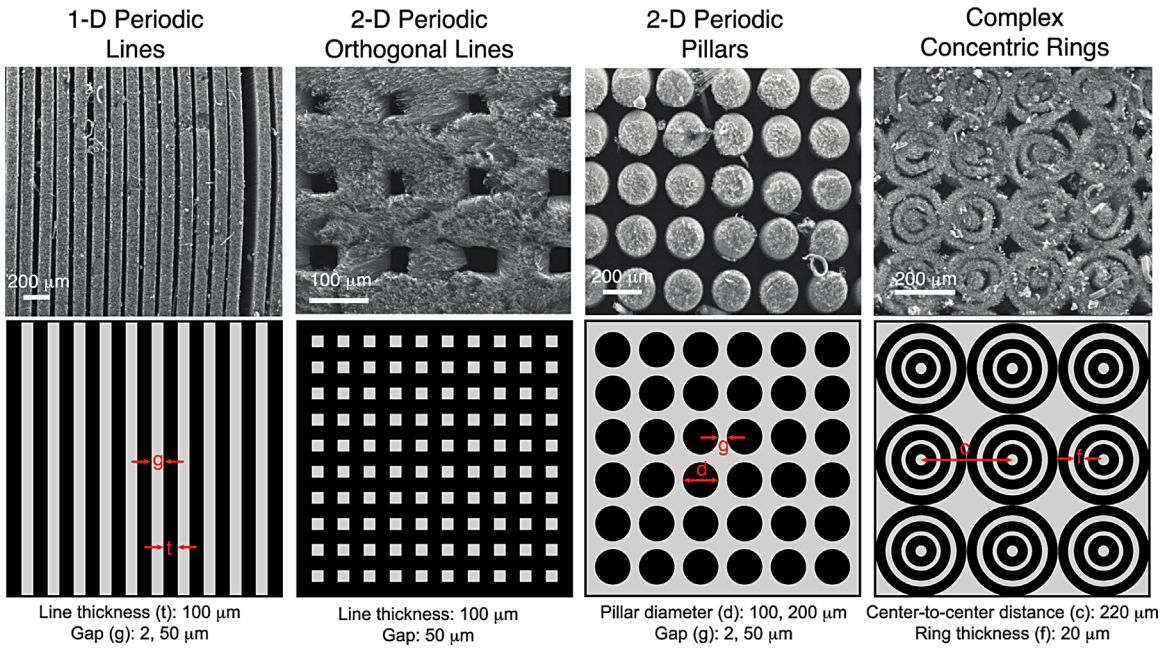

Fig. 1. Different geometrical patterns and corresponding SEM images of the fabricated VACNT foams. The dimensions of the different patterns are indicated under each image. (From left to right) SEM images of "lines 100 μm gap 50 μm," "orthogonal lines," "pillars 200 μm gap 50 μm," and "concentric rings."

response. Despite having the same density (0.0324 ± 0.02 g cm^{-3}), structures made of pillars with 100 μm diameters and 50 μm gaps exhibit a different mechanical behavior compared to that observed for the concentric ring columns, clearly demonstrating the fundamental role of geometry. The stress–strain curve measured for "pillars 100 gap 50 μm" is characterized by an initial linear regime, followed by a stress "plateau" (Figure 2a). Such foam-like behavior is also observed in patterns made by lines 100 μm thick separated by 50 μm gaps (0.045 ± 0.02 g cm^{-3}). Interestingly, the plateau stress (σ_{pl}, defined as the average stress between 15 and 25% strain during compression) measured in samples patterned by lines is higher than that observed for pillars, measuring 0.31 and 0.2 MPa, respectively.

As shown in Figure 2b, increasing the complexity of the structural architecture (from 1D to 2D periodic patterns) affects the stress–strain response. Up to $\epsilon = 0.2$, the 1D and 2D periodic structures have the same stress–strain behavior. At higher strain values, the stress of orthogonal line pattern increases steeply, while the 1D structure shows a stress "plateau" with positive slope. Importantly, the orthogonal lines exhibit a full recovery of the deformation. Figure 2a and b shows that the stress–strain behavior of pillars and lines is affected by the gap values (varied between 50 and 2 μm). At an impact velocity of 0.95 m s^{-1} (impact energy = 2.35 mJ; impact momentum = 4.94 mN s), the pattern made of pillars with diameter of 100 μm and gap of 2 μm reaches a strain of 0.3 and a peak stress of 1 MPa. In samples with patterns with a larger gap (50 μm), the strain and the peak stress are 0.45 and 0.48 MPa, respectively. Contrary to what was observed for patterns composed of pillars, the peak stress reached by lines with small gap (2 μm) is lower than the peak stress reached by lines with large gap values (50 μm).

The role of the geometry on the hysteretic energy dissipation is also shown in Figure 2a and b, and summarized in Table 1. The ability to dissipate energy (i.e., the area enclosed by the hysteresis loop) improves in the micro-patterned VACNT samples compared to non-patterned

Table 1. Mechanical properties of the samples tested with an impact velocity of 0.95 m s^{-1}.

Specimen	Theoretical effective density [g cm^{-3}]	Measured effective density [g cm^{-3}]	Energy dissipation [MJ m^{-3}]	Peak stress [MPa]	Max strain	Loading modulus [MPa]	SEA [kJ kg^{-1}]
VACNT forest	0.24	0.24	0.137	3.36	0.22	4.4	1.175
Lines 100 gap 2 μm	0.23	0.1 ± 0.03	0.085 ± 0.01	0.59 ± 0.08	0.36 ± 0.04	1.1 ± 0.12	1.103 ± 0.36
Lines 100 gap 50 μm	0.19	0.045 ± 0.02	0.17 ± 0.05	0.95 ± 0.09	0.52 ± 0.06	1.42 ± 0.03	4.35 ± 1.9
Orthogonal lines	0.231	0.0716 ± 0.03	0.15 ± 0.04	0.95 ± 0.2	0.45 ± 0.02	1.3 ± 0.3	2.4 ± 1.2
Pillars 100 gap 2 μm	0.184	0.08 ± 0.02	0.14 ± 0.03	0.84 ± 0.2	0.40 ± 0.11	1.39 ± 0.47	2.58 ± 0.32
Pillars 100 gap 50 μm	0.12	0.0324 ± 0.02	0.14 ± 0.05	0.53 ± 0.07	0.48 ± 0.02	1.14 ± 0.6	7.4 ± 4
Pillars 200 gap 50 μm	0.148	0.19 ± 0.05	0.18 ± 0.03	1.11 ± 0.05	0.46 ± 0.05	1.36 ± 0.5	1.11 ± 0.24
Concentric rings	0.167	0.032 ± 0.02	0.11 ± 0.01	1.26 ± 0.06	0.26 ± 0.14	5.9 ± 2	4.59 ± 2

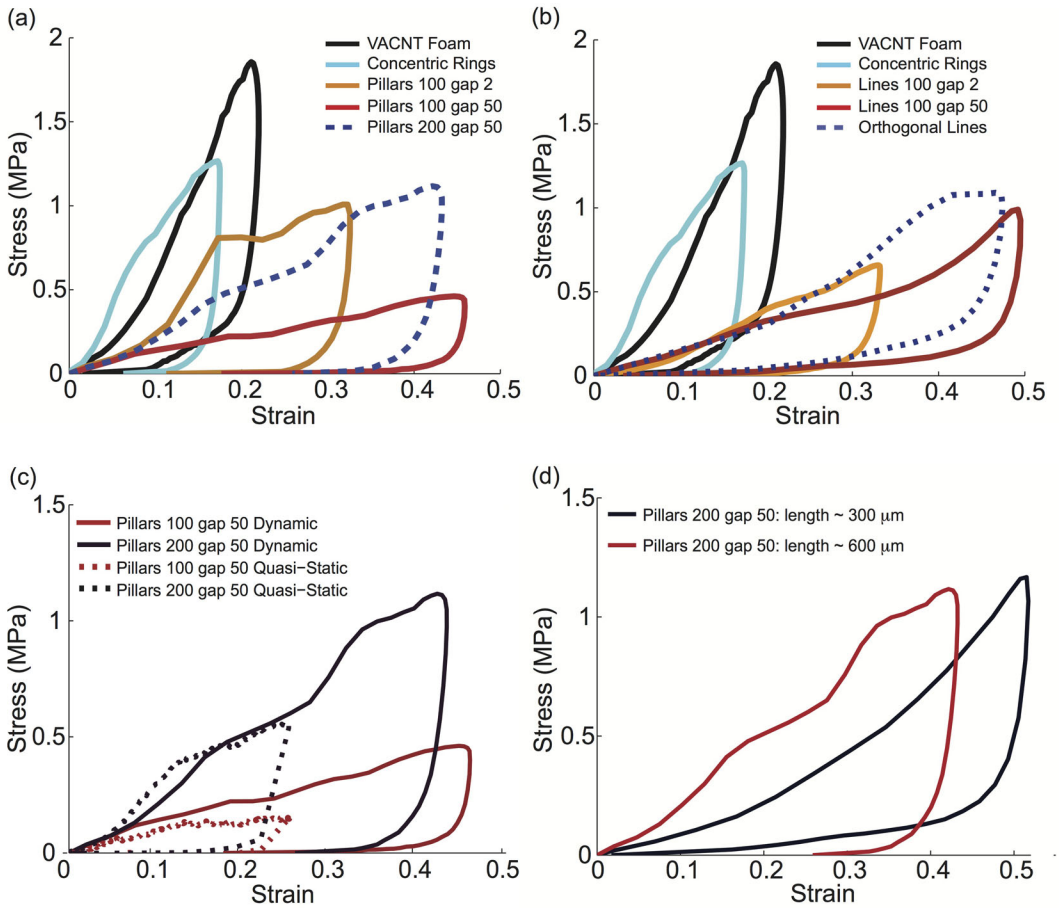

Fig. 2. Stress–strain curves of VACNT samples patterned with different geometrical microstructures. (a) Response of patterns containing different pillars compared with bulk VACNT foams and with VACNT foams patterned with concentric rings. (b) Response of patterns containing different lines compared with bulk VACNT foams and with VACNT foams patterned with concentric rings. (c) Effect of variations of the pillar's diameter on the quasi-static and dynamic response and (d) effect of the pillar's length on dynamic response.

VACNT forests. For example, by organizing VACNTs in pillars with diameter of 200 μm and gaps of 50 μm, the energy dissipation is increased up to ~1.7 times, and the peak stress decreases by ~3 times (compared to the same values for bulk foams). Changing the gap size between the lines from 2 to 50 μm increases the energy dissipation by up to ~2 times, while the peak stress increases by ~1.3 times.

Figure 2c shows the effect of the pillars' diameter on the quasi-static and dynamic mechanical response of the macrostructure. Both the peak stress and the energy dissipation increase as the pillar's diameter is increased (Figure 2c). Under impact loading, the peak stresses reached by structures made of pillars with diameter of 200 and 100 μm measure 1.17 and 0.45 MPa, respectively. The VACNT foams patterned with pillars with diameter of 200 μm dissipate 100% more energy than those structured with 100 μm diameter pillars. In quasi-static tests, the energy dissipated by pillars with larger diameter ($6.8 \times 10^6\,J\,m^{-3}$) is ~3 times higher than that measured for thinner pillars ($2.1 \times 10^6\,J\,m^{-3}$).

To control the sample's recovery, even after large deformations, we varied the length of the pillars (i.e., the overall thickness of the samples) by varying the precursor solution in the synthesis process, keeping all other parameters unchanged. 600 μm thick VACNT samples were fabricated using a 25 ml of precursor solution and 300 μm thick samples were obtained with 15 ml of precursor solution. Testing results (Figure 2d) show two main effects: (i) the slope of the initial segment of the stress–strain curve is significantly higher for longer pillars; (ii) upon unloading, the thinner samples (300 μm) show almost full recovery, while the 600 μm samples show lower recovery. The recoverability of VACNT arrays has been previously investigated and it is known to depend on the experimental testing setup, as well on the VACNT morphology.[10,21–23] A recent study showed that the amount of precursor solution used, and hence the total reaction time, largely affects the morphology, the density, and the alignment of VACNTs.[22] The tortuosity, the diameter, and the length of CNTs were found to increase as a function of the growth time.[22] These properties reflected on the mechanical response and on the resilience of the structure. Since both the structures (300 and 600 μm long pillars) exhibit the same deformation mechanism, we hypothesize that the better recoverability of the thinner samples is related to the different morphology and distribution of the CNTs within the pillars, although this was not investigated through SEM analysis.

The effect of the microstructural organization on the fundamental deformation mechanisms of the CNT structures was also investigated using high-speed microscopy during and after the impacts. The in-situ images reveal that samples with a gap value of 2 μm, consisting of both pillars (Supporting Information S1) and lines (Supporting Information S2), follow a uniaxial compression response. The high-speed image sequences suggest that the deformation initiates on the thin layer adjacent to the loading face (top of the CNT structure) and proceeds by sequential buckling at the opposite side of the microstructure (bottom of the CNT structure), a characteristic influence of the intrinsic density gradient in the VACNT structures.[10] As previously reported, the gradient in density characterizes all the CNT based structures, independently from their geometry.[10,16,21,24] Samples patterned with 50 μm gaps show a different microstructural deformation under impact tests compared to that observed in those with 2 μm gaps (Supporting Information S3). When impacted, the pillars undergo lateral deflection without exhibiting sequential buckling at the low density region (bottom). The deformation mechanism at the microscale might be compared to the buckling of an ideal column having one end fixed and the other end free to move laterally. The small lateral movements of the striker in the guide during impacts and the absence of lateral constrains at the force sensor–sample interface allow the top surface of the samples to slide laterally, while the opposite end (the bottom) is fixed to the silicon substrate. The results clearly show that the axial compressive impact force is higher than the critical load (or Euler buckling load)[25] and it causes an inelastic, permanent deflection that does not recover after unloading. This behavior can also explain the low overall recovery observed in samples patterned with pillars spaced by larger gaps (50 μm). When the gaps are small (2 μm), the lateral deflection of the pillars is prevented by pillar–pillar interactions, which act as lateral supports and provide mechanical reinforcement.

However, even samples with equal gaps (50 μm) but different geometries (lines and pillars) deform differently. The 1D organization of the lines and their dimensions result in a large, global shear deformation (the lines are 100 μm thick, ~800 μm tall, and ~4 mm long). Due to the gradient in density along the sample's thickness, an initially localized deformation (collective buckling) occurs at the bottom, low density region of the samples (Supporting Information S4). This initial non-affine deformation triggers a successive shear deformation of the whole structure. Such large shear deformation is not observed in patters with 2 μm gaps because of the mechanical constraint occurring when the lines start buckling. The high-speed image sequences show that the diameter has also an effect on the overall response of VACNT samples patterned with pillars. Under impact, the pillars with diameter of 200 μm and gap of 50 μm do not exhibit lateral deflection (as observed in pillars with 100 μm diameter), but they show uniaxial compression with the same characteristic sequential buckling as the one observed in bulk CNT forests and in micropatterned structures with small gap values (Supporting Information S5). The critical buckling load of the individual pillars in the patterns depends on the "effective" elastic modulus of the material composing them, the pillars diameter, and their length. The increase of the pillars diameter increases the moment of inertia, hence providing the structures with a higher critical buckling load. In addition, the number of CNTs nodes (defined as sites of interaction between individual CNTs in a given structure) is higher in the micropatterns made of pillars with diameter of 200 μm ($\rho = 0.19 \pm 0.05\,\mathrm{g\,cm^{-3}}$) compared to the patterns made of pillars with diameter of 100 μm ($\rho = 0.0324 \pm 0.02\,\mathrm{g\,cm^{-3}}$). A previous study has showed that the increase of the of node density correlates with the increase of the CNT structure density.[26] This might explain the higher energy absorption capacity of the pillars with larger diameter. While the "pillars 200 μm gap 50 μm" increase substantially the peak stress and the energy absorption capacity compared to "pillars 100 μm gap 50 μm," they do not enhance the specific energy absorption (SEA).

Table 1 provides the SEA of the CNT foams patterned with different structures and tested with an impact velocity of $0.95\,\mathrm{m\,s^{-1}}$. Results show that CNT foams organized in pillars with diameter of 100 μm and gap of 50 μm have the highest specific energy absorption, i.e., $\sim 7.4 \pm 4\,\mathrm{kJ\,kg^{-1}}$. Besides the high value of weight-specific energy absorption, such patterned structures show a constant plateau stress level (Figure 2a), a desirable feature for an energy absorbing material.

The complex geometry of the micropatterns made of columns of concentric tubes allowed us to obtain lighter structures preserving the high mechanical response observed in CNT bulk forest.[9] As previously reported, cylindrical tubes are a commonly used shape for high energy absorption, in which energy can be dissipated in several modes of deformation (e.g., concertina, diamond, Euler, tilting of tube axis, etc.).[27–31] An understanding of the material behavior at high strain rates in terms of failure and energy absorption capability is essential for predicting the impact performance of CNT structures patterned with columns of concentric tubes (Figure 3). The measured constitutive responses of these foams tested under different impact velocities are shown in Figure 3a (see also Supporting Information S6 and S7). Figure 3b and c reports selected image sequences acquired by the high-speed camera showing the buckling behavior of the columns, at different strain rates.

Quasi-static tests, carried out at a strain rate of $0.03\ \mathrm{s^{-1}}$ (Figure 3a), show an initial elastic region up to ~2.5% strain, followed by a long plateau region. Dynamic tests at impact velocities of $0.95\,\mathrm{m\,s^{-1}}$ (impact energy = 2.35 mJ; impact momentum = 4.94 mN s) and $2.56\,\mathrm{m\,s^{-1}}$ (impact energy = 17.03 mJ; impact momentum = 13.31 mN s) show a different stress–strain behavior, exhibiting an increase in the measured stress. For example, the plateau stress reached by concentric rings under impact tests is significantly higher than the plateau stress measured in quasi-static tests. At high impact

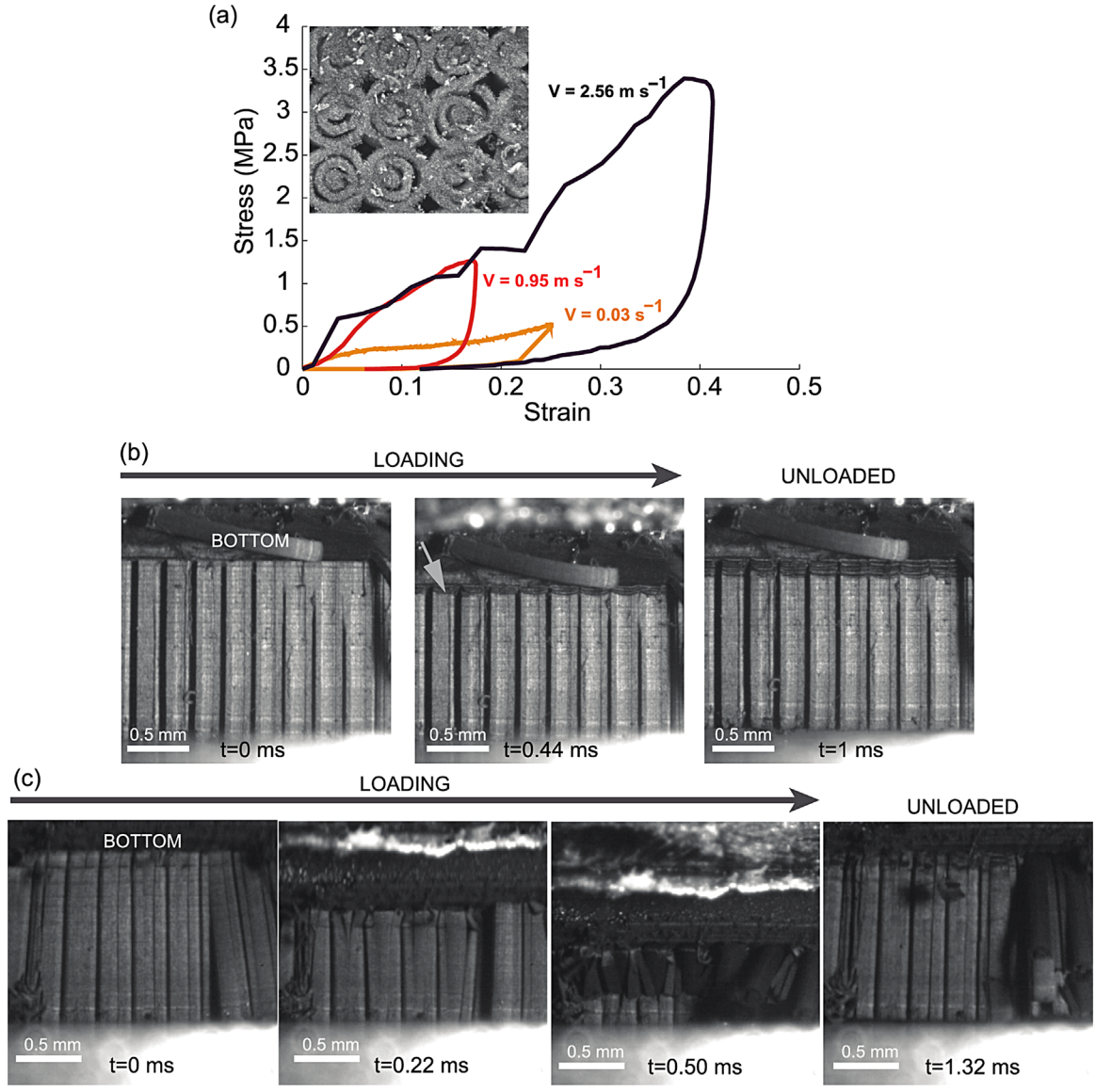

Fig. 3. (a) Stress–strain curves of concentric rings at different strain rates. Deformation mechanism of concentric rings at the impact velocity of (b) 0.95 m s^{-1} and (c) 2.56 m s^{-1}.

velocity (2.56 m s^{-1}), the concentric rings dissipate 0.6 MJ m^{-3}, while at 0.95 m s^{-1}, the energy dissipated is 0.1 MJ m^{-3}. The specific damping capacity measured at the same impact velocities is compared with the quasi-static data. At impact velocities of 0.95 and 2.56 m s^{-1}, the specific damping capacity of the samples patterned with concentric rings measures 0.9, while it is 0.5 for the quasi-static tests. The lower specific damping capacity measured in quasi-static, compared with the dynamic results, suggests strain-rate sensitivity in the materials' response.

Figure 3b and c reports in-situ experimental observations of the buckling of foams patterned with concentric tubes, under dynamic loading conditions. Despite the different stress–strain responses, the concentric tubes under quasi-static and dynamic loads (0.95 m s^{-1}) always collapse forming progressive buckles, which develop at the bottom of the structure (in the low density region of the VACNTs), as shown in Figure 3b. The buckling observed is permanent, as the folds do not recover when unloaded. This suggests that at the impact velocity of 0.95 m s^{-1}, the buckling is still driven by the nanostructure (the aligned CNTs of the column collapse into folds).

The high-speed image sequence of the microstructure at different stages of crushing shows that at higher impact velocity, 2.56 m s^{-1} (impact energy = 17.03 mJ; impact momentum = 13.31 mN s), the columns exhibit a much larger deformation and a global buckling mode (Figure 3c). This suggests that at the highest impact velocity the buckling is driven by the microstructural geometry. The buckling starts close to the low density region (bottom) of the column in a fold with a wavelength higher than that observed in columns impacted at lower impact velocity. As compression progresses, a second fold develops just next to the first one. With further compression, the strain localizes close to the

mid-height of the column, causing a global structural buckling of the columns. Interestingly, despite the pronounced buckling, the columns recover ~75% of their original shape.

To study the impact absorption efficiency of the patterned VACNT microstructures, we calculated the dynamic cushion factor (C_{dyn}) and plotted this value against the maximum strain (ϵ_{max}). The cushion factor as a function of the maximum strain was calculated for the impact velocities of 0.95 and 2.56 m s^{-1}, shown in Figure 4a and b, respectively. Both an increase in energy absorption and decrease in the peak stress contribute to decrease the cushion factor, which is desirable for impact protection. At the lower impact velocity (0.95 m s^{-1}; impact energy = 2.35 mJ; impact momentum = 4.94 mN s), VACNT foams patterned with 1D and 2D periodic arrays exhibit improved cushioning (Figure 4a).

Compared to non-patterned VACNT forests samples, the line arrays (1D), and pillars and orthogonal line arrays (2D) deform more at moderate stress levels. The increased energy absorption due to the large deformations at moderate stress levels contributes to a reduction in the cushion factors. In contrast, the complex structure of concentric rings exhibits a higher cushion factor due to lower deformation and higher peak stress reached during testing. However, the cushioning performance of concentric ring columns exhibit the best performance at higher impact velocity (2.56 m s^{-1}; impact energy = 17.03 mJ; impact momentum = 13.31 mN s), whereas the other samples of 1D and 2D arrays of lines and pillars reached their performance limit, deforming beyond the densification strain (Figure 4b). It should be noted that the concentric ring columns deformed only 40% at 2.56 m s^{-1} and have the capacity to cushion much higher velocities of impacts. In Figure 5, we compare the specific energy absorption of the patterned VACNT foams, impacted at the velocity of 2.65 m s^{-1}, to that of existing impact absorbing materials at full compaction (i.e., metal/polymer cellular structures,[32] sandwiches,[33] tubes[34–36]).

At high impact velocity, the VACNT foams patterned with concentric rings have a more competitive SEA than existing energy absorber materials. The synthetic foams based on an aluminum matrix[37] and the polymer foams reinforced with small carbon fiber-reinforced epoxy tubes[34] outperform the CNT concentric rings; however, the high specific energy absorption correlates to higher values of their density (Figure 5).

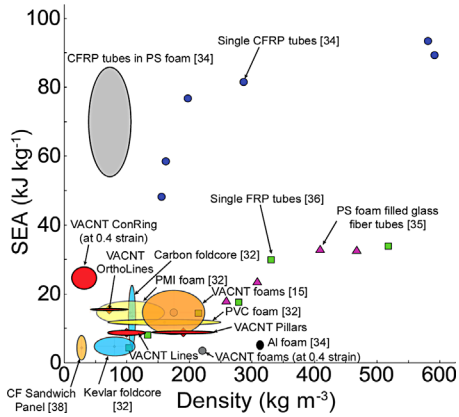

Fig. 5. Specific energy absorption (SEA) values of VACNT microstructures and other existing impact absorber materials.

It is important to note that, contrary to all other structures, the SEA of VACNT foams patterned with concentric rings is measured at the maximum strain of 0.4, and not during their full compaction. This is due to the fact that the concentric rings reached a deformation of ~0.4 at the impact velocity of 2.56 m s^{-1} (impact energy = 17.03 mJ; impact momentum = 13.31 mN s), and we calculated the energy absorbed up to this deformation value. Therefore, the concentric rings will exhibit much higher SEA when they are deformed fully at much higher impact velocities. In addition, the in-situ videos reveal their almost full recovery and the absence of permanent damage, whereas all other materials/structures in Figure 5 undergo permanent failure. The results show that the SEA is strongly dependent on the microstructural organization of the VACNT foams and on the impact velocity. Finally, the results demonstrate that variations in the geometry of the micro-architectures can be used to control the impact performance of CNT foams in a broad design space, which can be made to

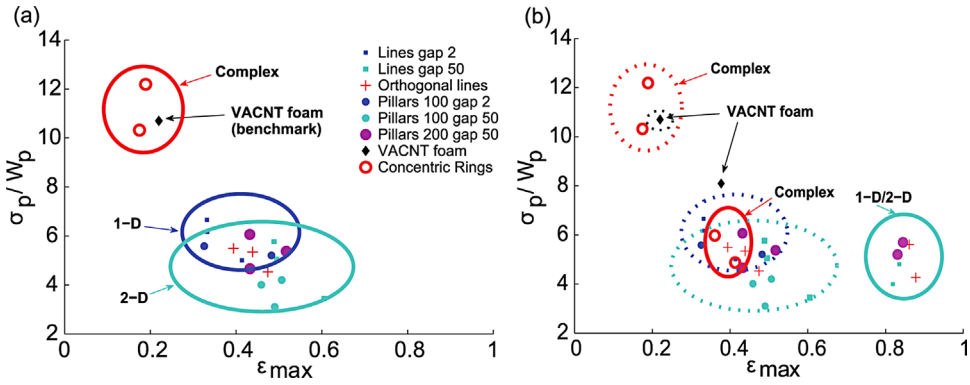

Fig. 4. Plot of the Cushion factor (σ_p/W_p) as a function of the maximum strain (ϵ_{max}) for patterned and non-patterned structures at the impact velocity of (a) 0.95 m s^{-1} and (b) 2.56 m s^{-1}.

address specific applications. Such extremely lightweight materials, characterized by high stiffness, strength, and energy absorption capacities, are very attractive for weight sensitive applications (i.e., automotive and aerospace applications).

3. Conclusion

We present the fabrication and the bulk dynamic characterization of new foam materials consisting of micropatterned VACNT forests. The patterning results in materials with significantly reduced bulk density, but with similar, or up to an order of magnitude improved, dynamic performance (considering peak stress and energy absorption capacity). The geometry of the microstructural architectures and the impact velocity (loading rate) largely affect the deformation mechanisms and the bulk stress–strain response of these materials. In particular, changes in the microscale geometry of the patterns allowed tuning the specific energy absorption (SEA) of VACNTs under impact loading. By organizing VACNTs in concentric ring columns, for example, we obtained a value of SEA $>25\,\mathrm{kJ\,kg^{-1}}$ that is competitive with that of existing energy absorbers described in literature. The patterned VACNT foams described in this work hold great potential as novel lightweight material for impact protection.

4. Experimental Section

VACNT structures were grown on patterned silicon wafers using a floating catalyst thermal chemical vapor deposition (tCVD) process, as reported previously.[9,11] The micropatterns on the substrate were realized using photolithographic techniques as follows: a hexamethyldisilazane (HDMS) primer was deposited by evaporation for 300 s on a silicon wafer previously dehydrated at 130 °C on a hot plate for 60 s. AZ-positive photoresist was spin-coated on the substrates, which were then exposed to UV light under a mask with desired geometry (Figure 1) for 3 s at 330 W. The substrate was then immersed into a developer bath and subsequently, a chromium thin film was evaporated onto its surface using an electron beam evaporator. Finally, the wafer was washed in acetone to remove the undeveloped photoresist, leaving the chromium thin film where CNT growth was not desired. The fabricated samples had a cross-sectional area of $20.63 \pm 6\ \mathrm{mm^2}$ and a thickness of $\sim 727 \pm 300\ \mu\mathrm{m}$. The orientation and alignment of CNT forests grown by floating catalyst CVD method have been examined in the past and have been found to vary along the height of the structure (with CNTs aligned at the bottom and along the length of the forest, and highly entangled and tortuous at the top).[39] The SEM images (Supporting Information S8) of the CNTs at the top and at the mid-height of pillars confirm that the change in the alignment and the density gradient typical of the VACNT forests is also observed when CNTs are synthetized on substrates patterned with different growth templates (e.g., circles). The pattern's geometry determines the effective bulk density of the microstructures, which was obtained by dividing the measured weight by the sample's volume. The theoretical effective densities of different structures were calculated by multiplying the bulk density of the VACNT forest by the filling fraction of the patterns ($A_{\mathrm{CNT}}/A_{\mathrm{sample}}$, where A_{CNT} is the area occupied by the CNTs and A_{sample} is the area of the silicon substrate).

To characterize their mechanical behavior, both quasi-static and dynamic compression tests were carried out on all samples. The quasi-static tests were performed using an Instron E3000 electropulse testing system, at a constant strain rate of $0.03\ \mathrm{s^{-1}}$ and up to a maximum compressive strain of 0.25. The energy absorption was computed by calculating the area within the hysteresis loop in the stress–strain curve. The experimental setup used for the impact tests consists of three main components:[40] (i) a flat-plunge striker with mass, $m = 5.2\,\mathrm{g}$; (ii) a dynamic force sensor for measuring the transient force history; and (iii) a high-speed microscope for in-situ visualization and dynamic displacement measurements. The patterned CNT foams, still attached to the silicon substrates, were glued to the flat-plunge striker using a double-sided copper tape on the substrate side. The striker was launched on a frictionless guide using a pneumatic cylinder, such that the VACNT specimens directly impacted the force sensor. A quartz impact force sensor (PCB Piezotronics) recorded the transient force-time history during impact. A high-speed camera (Vision Research's Phantom V1610) coupled to a microscopic lens (Infinity) and operated at 100,000 frames per second was used for in-situ visualization of the microscale dynamic deformation during the impact. The dynamic displacement time history was obtained by post-processing the high-speed image sequence using commercial digital image correlation software (Image system's TEMA). The recorded dynamic displacement- and force-time histories were then used to obtain the dynamic stress–strain response of the CNT foams subjected to impact loading. We divided the force by nominal cross-sectional area of the bulk sample to obtain the nominal stress, and divided the displacement by the sample height to calculate the nominal strain. To study rate effects, we used two different impact velocities, $0.95\,\mathrm{m\,s^{-1}}$ (impact energy $= 2.35\,\mathrm{mJ}$; impact momentum $= 4.94$ mN s) and $2.56\,\mathrm{m\,s^{-1}}$ (impact energy $= 17.03\,\mathrm{mJ}$; impact momentum $= 13.31$ mN s).

From the dynamic constitutive (stress–strain) response obtained, we extracted several material properties such as loading modulus, peak stress, maximum deformation, energy dissipation, cushion factor, and percentage recovery. The loading modulus was obtained by examining the initial slope of the stress–strain curve, while the energy dissipated was calculated by integrating the area of the hysteresis loop of each loading cycle. The dynamic cushion factor (C_{dyn}) was obtained by using Equation 1, where σ_p is the peak stress and W_p is the energy absorbed up to that stress,[5]

$$C_{dyn} = \frac{\sigma_{\mathrm{p}}}{W_{\mathrm{p}}} \tag{1}$$

High-speed imaging of microscale deformation provides insights into the fundamental deformation mechanisms involved in different length and time scales.

To evaluate the rate sensitivity on the energy dissipation, the specific damping capacity (D; Equation 2)[41] was calculated in quasi-statics and dynamics for the patterns made by concentric rings.

$$D = \frac{\Delta U}{U} \tag{2}$$

$$\Delta U = \oint \sigma d\epsilon \tag{3}$$

$$U = \int_0^{\sigma_{\max}} \sigma d\epsilon \tag{4}$$

Here, ΔU is the dissipated energy (Equation 3), U is the elastic energy (Equation 4), σ is the stress, and ϵ is the strain. To compare the energy absorption capabilities and the influence of the effective density measured in CNT structures with different patterns' geometry, the specific energy absorption (SEA) was calculated dividing the total energy absorbed up to the peak stress by the mass (m) of the specimen (Equation 5).

$$\mathrm{SEA} = \frac{\int_0^{\sigma_{\max}} \sigma d\epsilon}{m} \tag{5}$$

[1] F. Xia, L. Jiang, *Adv. Mater.* **2008**, *20*, 2842.
[2] M. Sarikaya, I. A. Aksay, *Biomimetics, Design and Processing of Materials, AIP Series in Polymers and Complex Materials*, Woodbury, New York, **1995**.
[3] P. Y. Chen, A. Y. M. Lin, Y. S. Lin, Y. Seki, A. G. Stokes, J. Peyras, E. A. Olevsky, M. A. Meyers, J. McKittrick, *J. Mech. Behav. Biomed.* **2008**, *1*, 208.
[4] J-H. Lee, J. P. Singer, E. L. Thomas, *Adv. Mater.* **2012**, *24*, 4782.
[5] L. J. Gibson, M. F. Ashby, *Cellular Solids*, Cambridge University Press, New York, **2010**.
[6] T. A. Schaedler, A. J. Jacobsen, A. Torrents, A. E. Sorensen, J. Lian, J. R. Greer, L. Valdevit, W. B. Carter, *Science* **2011**, 334.
[7] D. Jang, L. R. Meza, F. Greer, J. R. Greer, *Nat. Mater.* **2013**, *12*, 893.
[8] J-H. Lee, L. Wang, M. C. Boyce, E. L. Thomas, *Nano Lett.* **2012**, *12*, 4392.
[9] L. Lattanzi, L. De Nardo, J. R. Raney, C. Daraio, *Adv. Eng. Mater.* **2014**, *15*, 1.
[10] A. Cao, P. L. Dickrell, W. G. Sawyer, M. N. Ghasemi-Nejhad, P. M. Ajayan, *Science* **2005**, *310*, 1307.
[11] L. Lattanzi, J. R. Raney, L. De Nardo, A. Misra, C. Daraio, *J. Appl. Phys.* **2012**, *111*, 074314.
[12] A. Misra, J. R. Greer, C. Daraio, *Adv. Mater.* **2009**, *21*, 334.
[13] J. Suhr, P. Victor, L. Ci, S. Sreekala, X. Zhang, O. Nalamasu, P. M. Ajayan, *Nat. Nanotechnol.* **2007**, *2*, 417.
[14] O. Yaglioglu, A. Cao, A. J. Hart, R. Martens, A. H. Slocum, *Adv. Funct. Mater.* **2012**, *22*, 5028.
[15] J. R. Raney, A. Misra, C. Daraio, *Carbon* **2011**, *49*, 3631.
[16] R. Thevamaran, E. R. Meshot, C. Daraio, *Carbon* **2015**, *84*, 390.
[17] C. Daraio, V. F. Nesterenko, S. Jin, *Appl. Phys. Lett.* **2004**, *85*, 5373.
[18] A. G. Hanssen, M. Langseth, O. S. Hopperstad, *Int. J. Mech. Sci.* **2001**, *43*, 153.
[19] M. R. Maschmann, Z. Qiuhong, D. Feng, D. Liming, J. Baur, *Carbon* **2011**, *49*, 386.
[20] A. Misra, J. R. Raney, A. E. Craig, C. Daraio, *Nanotechnology* **2011**, *22*, 425705.
[21] S. B. Hutchens, L. J. Halland, J. R. Greer, *Adv. Funct. Mater.* **2010**, *20*, 2338.
[22] S. Pathak, J. R. Raney, C. Daraio, *Carbon* **2013**, *63*, 303.
[23] M. R. Maschmann, Q. Zhang, R. Wheeler, F. Du, L. Dai, J. Baur, *ACS Appl. Mater. Interfaces* **2011**, *3*, 648.
[24] O. Yaglioglu, *PhD Thesis*, Massachusetts Institute of Technology, June **2007**.
[25] Z. P. Bazant, L. Cedolin, *Stability of Structures*, Dover, New York, **2003**.
[26] M. Xu, D. N. Futaba, M. Yumura, K. Hata, *Nano Lett.* **2011**, *11*, 3279.
[27] A. A. A. Alghamdi, *Thin Wall. Struct.* **2001**, *39*, 189.
[28] D. Karagiozova, M. Alves, *Int. J. Solids Struct.* **2004**, *41*, 1565.
[29] A. Abdul-Latif, R. Baleh, *J. Appl. Mech.* **2008**, *75*, 031013.
[30] S. R. Raid, *Int. J. Mech. Sci.* **1993**, *35*, 1035.
[31] K. R. F. Andrews, *Int. J. of Mech. Sci.*, **1983**, *25*, 687.
[32] S. Heimbs, First International Workshop on Hydraulic Equipment and Support Systems for Mining, Huludao, China, August **2012**.
[33] L. L. Yan, B. Han, B. Yu, C. Q. Chen, Q. C. Zhang, T. J. Lu, *Mater. Design* **2014**, *60*, 510.
[34] R. A. Alia, W. J. Cantwell, G. S. Langdon, S. C. K. Yuen, G. N. Nurick, *Compos. Part B* **2014**, *61*, 127.
[35] F. Tarlochan, S. Ramesh, S. Harpreet, *Compos. Part B* **2012**, *43*, 2198.
[36] L. Yan, N. Chouw, *Mater. Design* **2013**, *51*, 629.
[37] X. F. Tao, Y. Y. Zhao, *Scripta Mater.* **2009**, *61*, 461.

[38] J. Xiong, A. Vaziri, L. Ma, J. Papadopoulos, L. Wu, *Compos. Struct.* **2012**, *94*, 793.
[39] M. Pinault, V. Pichot, H. Khodja, P. Launois, C. Reynaud, *M. M. L'Hermite, Nano Lett.* **2005**, *5*, 2394.
[40] R. Thevamaran, C. Daraio, *Exp. Mech.* **2014**.
[41] M. F. Ashby, *Materials Selection in Mechanical Design*, Elsevier, Oxford, England, **2005**.